

Integrating simultaneous interfacial shear rheology with neutron reflectometry for structural and dynamic analysis of fluid interfacial systems

Pablo Sánchez-Puga,^{a*‡} Javier Tajuelo,^b Javier Carrascosa-Tejedor,^a Miguel Ángel Rubio,^c Philipp Gutfreund^a and Armando Maestro^{d,e}

Received 28 October 2025

Accepted 25 February 2026

Edited by F. Meneau, Brazilian Synchrotron Light Laboratory, Brazil

‡ Present address: Department of Physics and Astronomy, Uppsala University, Box 516, Uppsala S-751 20, Sweden.

Keywords: neutron reflectometry; interfacial rheology; Langmuir films.

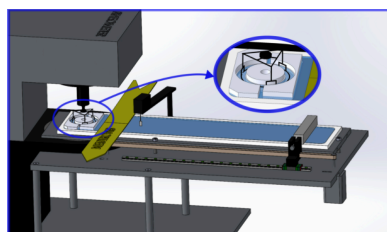
Supporting information: this article has supporting information at journals.iucr.org/j

^aInstitut Laue–Langevin, 38042, Grenoble, France, ^bDepartamento de Física Interdisciplinar, Facultad de Ciencias, Universidad Nacional de Educación a Distancia (UNED), 28232, Las Rozas, Spain, ^cDepartamento de Física Fundamental, Facultad de Ciencias, Universidad Nacional de Educación a Distancia (UNED), 28232, Las Rozas, Spain, ^dCentro de Física de Materiales (CFM-MPC), CSIC-EHU, Paseo Manuel de Lardizabal 5, 20018, Donostia-San Sebastián, Spain, and ^eIKERBASQUE, Basque Foundation for Science, Bilbao, Spain. *Correspondence e-mail: pablo.sanchez-puga@physics.uu.se

The study of the structure and mechanical properties of complex fluid interfaces has attracted growing interest in recent decades due to its fundamental relevance to biological systems, drug development and industrial applications. A central challenge in this field is establishing a direct link between the macroscopic mechanical response of an interface and its underlying molecular-scale structural evolution. To address this, we present an integrated experimental approach that combines interfacial rheology with neutron reflectometry, enabling simultaneous measurement of dynamical and structural properties on the same sample. This strategy eliminates the uncertainties inherent in comparing separately prepared samples and, more importantly, provides direct mechanistic insight into phenomena such as film formation, phase transitions and kinetic processes. We validated the methodology using Langmuir monolayers of the saturated phospholipid 1,2-dipalmitoyl-*sn*-glycero-3-phosphocholine at the air/water interface. The measurements were performed using a newly developed sample environment for the FIGARO horizontal neutron reflectometer at the Institut Laue–Langevin, which integrates a double wall–ring interfacial shear rheometer compatible with commercial rotational rheometers. This innovative setup paves the way for broad application to complex interfacial systems (including polymers, biomembranes and multi-layer films), where coupled structural–mechanical insight is critical.

1. Introduction

Fluid interfaces are found in living systems and various technological processes. Currently, significant scientific effort is being devoted to exploring the potential of supramolecular assemblies composed of large, multifunctional colloidal nano-objects, which encompass amphiphilic molecules, macromolecules, polymers, and organic and metallic nanoparticles (Guzmán *et al.*, 2016; Maestro, 2019; Guzmán *et al.*, 2022). These interfaces often exhibit complex structural organization, displaying a non-linear response to mechanical deformations (Fuller & Vermant, 2012). The interrelationship between the structural and dynamical characteristics of these complex fluid interfaces is crucial in numerous natural and technological processes (López-Díaz *et al.*, 2020). Increasing our knowledge of these phenomena is essential for understanding the fundamentals of various biological processes, the development of new drugs and consumer products, and other industrial applications (Maestro, 2019). Examples of such complex interfaces are the phospholipid bilayer that composes



cell membranes together with the inclusion of other chemical compounds (cholesterol, proteins, fatty acids *etc.*) (Waldie *et al.*, 2020), the pulmonary surfactant (Collada *et al.*, 2026) and the tear film. In addition, interfaces are inherent to many products in the food, personal care and biotherapeutic sectors, where emulsions and foams are ubiquitous (Maestro *et al.*, 2014; Maestro *et al.*, 2018).

Several scattering techniques have been developed so far to address interfacial molecular structures (Kaganer *et al.*, 1999). In particular, neutron reflectometry (NR) and X-ray reflectometry (XRR) (Braun *et al.*, 2017; Lu *et al.*, 2000; Maestro & Gutfreund, 2021), together with grazing-incidence X-ray diffraction (GIXD) (Gerber *et al.*, 2006; Daillant & Gibaud, 2008; Krafft *et al.*, 2001), have been successfully used to reveal both the in-plane and out-of-plane molecular structures of surface films. XRR offers the advantage of covering a broad range of length scales, enabling high-resolution measurements, while GIXD allows the extraction of fine details of the crystallographic morphology at the molecular scale. However, their high flux density and electronic interaction can be detrimental to various soft matter systems. In contrast, NR, while not covering the same momentum transfer range as XRR, provides the unique advantage of allowing scattering contrast variation, achieved through sample deuteration or the use of mixtures of light and heavy water, in the case of aqueous solutions. Furthermore, NR is considerably less invasive compared with XRR, making it more suitable for the study of delicate soft matter samples.

In addition to large-scale facility-based techniques, other approaches have been used to characterize the microstructure in the plane of fluid interfaces, such as atomic force microscopy (Gonzalez-Martinez *et al.*, 2019a; Gonzalez-Martinez *et al.*, 2019b), ellipsometry (Nestler & Helm, 2017; Maestro *et al.*, 2015; Ducharme *et al.*, 2001; Maestro & Gutfreund, 2021), fluorescence microscopy (Vutukuri *et al.*, 2020; Beltramo & Vermant, 2016) or Brewster angle microscopy (Rivière *et al.*, 1994; Carrascosa-Tejedor *et al.*, 2022; Carrascosa-Tejedor *et al.*, 2023). These are of great interest as complementary techniques to observe the formation of domains above the micrometre scale.

With regard to interfacial rheology, several instruments have been designed for the study of the dynamical behaviour of interfaces. For shear deformation, examples include several interfacial shear rheometers (ISRs) such as the magnetic needle ISR (Brooks *et al.*, 1999; Tajuelo *et al.*, 2015; Tajuelo *et al.*, 2016), the microbutton (Zell *et al.*, 2016), and specially designed fixtures for commercial rotational rheometers such as the conical bob (Erni *et al.*, 2003; Tajuelo *et al.*, 2017; Sánchez-Puga *et al.*, 2019) and the double wall–ring (DWR) (Vandebriel *et al.*, 2010). For dilatational measurements, achieving pure deformations in experiments is rather difficult. Barrier compression techniques in rectangular Pockels–Langmuir troughs impose mixed deformations because they induce changes in both the form and the area of the interface. Nevertheless, procedures have been devised to obtain rheological information from such measurements (Petkov *et al.*, 2000). Recently, experimental procedures to induce pure

dilatational deformations have been implemented in the ‘radial trough’, in its original form (Pepicelli *et al.*, 2017) or later versions (Kale *et al.*, 2021; Huang & Frostad, 2025) and Quadrotrough configurations (Tein *et al.*, 2022; Ashkenazi *et al.*, 2024).

Although some of the studies mentioned above on interfacial rheology include observations of the interface using microscopy, other work has specifically focused on combining optical and mechanical techniques to directly link mechanical and structural properties at the microscale in the context of particle-stabilized systems (Keim & Arratia, 2013; Barman & Christopher, 2016; Alicke *et al.*, 2023). These approaches provide valuable insight at the micrometre scale, while simultaneous access to molecular-level structural information can be achieved using scattering-based techniques.

Unless the interfacial flow is dominated by the interfacial drag on the probe, a circumstance that cannot be known *a priori*, adequately accounting for inertia effects and drag of the bulk phases, and properly separating elastic and viscous contributions of the interface response, are mandatory. Such tasks can be conveniently carried out in the case of shear rheometry measurements using flow field based data analysis schemes (FFBDA) (Reynaert *et al.*, 2008; Vandebriel *et al.*, 2010; Verwijlen *et al.*, 2011; Tajuelo *et al.*, 2015; Tajuelo *et al.*, 2016; Tajuelo *et al.*, 2017; Sánchez-Puga *et al.*, 2021).

Integration of molecular-level structural data with dynamical measurements from interfacial rheometry offers a comprehensive picture of interfacial systems and facilitates a more reliable interpretation of their mechanical response. This is the reason for the growing interest in the combination of NR and interfacial rheology (IR) experimental data (Tein *et al.*, 2022; Thompson *et al.*, 2025). From a practical point of view, the high sensitivity of interfacial systems to temperature, evaporation and other experimental conditions, especially if working near phase transitions or metastable states, makes it challenging to rigorously compare structural and rheological measurements performed on separate samples. Hence, the availability of experimental facilities that offer the possibility of performing simultaneous NR and IR measurements (Novaes-Silva *et al.*, 2025) is of primary importance for the study of interfacial systems.

In this work, we present an experimental setup that allows the integration of an interfacial shear rheometry system for simultaneous measurements on the FIGARO (Campbell *et al.*, 2011) horizontal reflectometer at the Institut Laue–Langevin (ILL), which is now available as an integrated sample environment for the interfacial science community. To our knowledge, there is no neutron or synchrotron facility worldwide that offers as a standard feature the possibility of making simultaneous structural and high-sensitivity dynamical shear measurements on the same fluid–fluid interface sample.

This paper is organized in two main sections. Section 2 provides a description of the DWR design and data acquisition and analysis methodology, while Section 4 focuses on the device’s performance, including experimental validation using a 1,2-dipalmitoyl-*sn*-glycero-3-phosphocholine (DPPC) monolayer at the air/water interface, whose structure and dynamical

behaviour have been previously reported in separate experiments (Hermans & Vermant, 2014; Campbell *et al.*, 2018; Carrascosa-Tejedor *et al.*, 2020).

2. Design, operation and data analysis

2.1. Experimental setup

Langmuir trough and support system. The mechanical setup designed for the FIGARO beamline at the ILL, as shown in Fig. 1, includes a custom-designed Langmuir trough featuring a single moving barrier, which has been integrated with a commercial Anton Paar MCR702e space rheometer through an auxiliary support table system. The trough, machined on a single polytetrafluoroethylene plate and mounted on an aluminium plate, incorporates a copper tube circuit at its base that can be connected to a thermostatic bath, ensuring accurate temperature regulation of the sample.

The mobile barrier, made of polyoxymethylene, traverses the Langmuir trough's top via a carriage mechanism on a rail, driven by a stepper motor attached to a toothed belt. The trough itself measures 101 mm in width, and the barrier's 450 mm travel range allows for compression ratios slightly above 5. An interfacial pressure sensor/microbalance

(Kibron) equipped with a 4 mm wide Wilhelmy plate is used for the measurement and control of the interfacial pressure.

DWR interfacial shear rheometer. The DWR geometry comprises two main components (Vandebriel *et al.*, 2010): the double wall annular cell, placed in the Langmuir trough, and the ring probe fixture for the commercial Anton Paar rotational rheometers, available at the ILL. The double wall annular cup (see Fig. 2), custom-made of polytetrafluoroethylene, has a double-step radial profile (inner with radius $R_i = 20$ mm, and outer with radius $R_o = 28.79$ mm) to minimize meniscus effects and ensure interface pinning at the edges of the steps. The double wall annular cell is positioned at the trough's back-end and has two openings, orientated transversely to the barrier motion direction, designed to facilitate a smooth and symmetric entry of interfacial flow into the annular double wall channel. The symmetry axis of the double wall channel is carefully aligned with the rheometer's probe rotation axis. The geometric parameters of the double wall and the ring have been selected in order to (i) make the values of the interfacial shear strain at the inner and outer contact lines at the ring surface as close to each other as possible, and (ii) make the distances between the ring and the walls (3 mm or more) slightly larger than the air/water capillary length (~ 2.7 mm).

The ring probe has been manufactured using titanium 3D printing technology (3D Systems, Leuven, Belgium), adopting a diamond-shaped cross section (Vandebriel *et al.*, 2010; Hermans & Vermant, 2014) with 1 mm diagonal. The ring probe is not a closed circle but has three small openings, equally spaced in the angular coordinate, to allow for the inner and outer interfacial regions to be at the same interfacial pressure. The ring probe fixture incorporates a specialized top

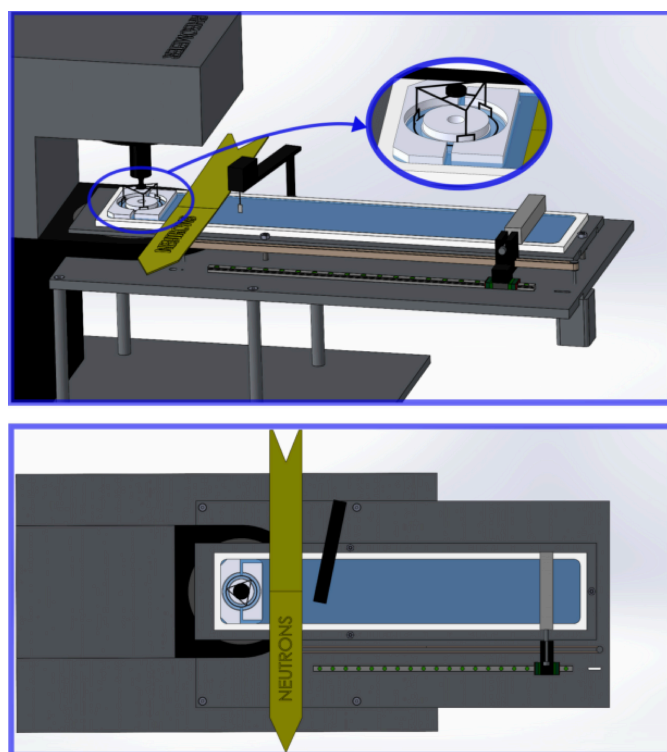


Figure 1

Sketch of the DWR on the FIGARO setup. (a) Perspective of the whole ensemble attached to the rheometer frame including the support table. (Inset: detail of the DWR ensemble.) (b) Top view with a half-height cutting plane showing the disposition of the interfacial rheology measurement system, incident neutron beam and footprint, interfacial pressure balance position, and barrier travel range.

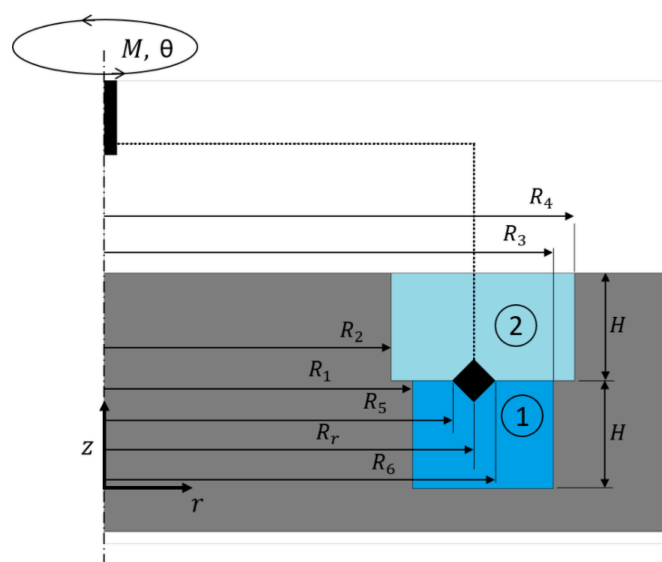


Figure 2

Sketch of the DWR cross-sectional geometry. Only the right half is shown, taking advantage of the rotational symmetry to highlight the details. The different radii are labelled as done by Sanchez-Puga & Rubio (2025a).

connection which enables seamless, backlash-free integration with disposable system shafts, ensuring compatibility with Anton Paar rheometers available at the ILL. Accurate centring of the ring probe in the double wall annular cell is facilitated by the circular shape of the top part of the inner-wall section of the shear cell.

Integration on FIGARO. The considerable length of the trough and the specific horizontal and vertical positioning requirements, necessary for it to be properly accommodated on the neutron instrument's anti-vibration table, demanded the building of an auxiliary support table. This support table has three legs. The leg placed furthest from the rheometer rests on an additional plate designed to extend the support surface. This plate effectively enlarges the support area provided by FIGARO's anti-vibration table, ensuring stable and level placement of the trough during measurements.

The neutron beam incidence area has a footprint at the interface 40–60 mm wide and 80 mm long in the longitudinal and transverse directions to the Langmuir trough, respectively (see Fig. 1). Then the Langmuir trough is placed so that there is a 10 mm gap between the end of the annular shear channel ensemble and the beam footprint, in order to minimize possible meniscus effects. Similar 10 mm gaps were allowed between the neutron beam footprint and the Wilhelmy plate and the mobile barrier at the maximum compression position.

Finally, a cabin has been constructed to ensure optimal control of the experimental conditions. The cabin is equipped with lateral quartz windows to facilitate the entry and exit of incident and reflected beams. In addition, the upper wall of the cabin supports a horizontal optical glass window. A laser beam enters the cabin through that window and is used for precise measurement of the vertical distance between the interface and a reference element. This cabin+laser positioning system

allows for precise control of the vertical positioning of the interface under study, prevents sample contamination and enhances the control over the ambient thermodynamic conditions, basically air temperature and relative humidity.

2.2. Electrical connections and data acquisition

In this section, we provide an overview of the electrical connection scheme. Fig. 3 illustrates the connections of the interfacial rheology measurement system and the Langmuir trough, both controlled by the same computer.

The Anton Paar MCR702 torsion rheometer used here offers the possibility to configure four analogue output signals ($\pm 10\text{ V}$ and 16 bit resolution) with selectable gain values according to the user's requirements. In the setup described here, four signals are acquired simultaneously: the angular displacement (gain = 600 V rad^{-1}), two torque signals with different gains (5×10^4 and $5 \times 10^5\text{ V Nm}^{-1}$, respectively) and a trigger signal indicating the start of each measurement interval. The two torque signals correspond to the same transducer but are read through separate amplification channels to allow accurate measurements across different orders of magnitude. This trigger signal is used to detect the beginning of a new waveform corresponding to a different measurement to be analysed and stored as raw data for security. These four analogue signals are acquired through a USB data acquisition (DAQ) board (Digilent MCC USB-234; 8 SE/4 DIFF analogue inputs; 16-bit resolution, 100 kS s^{-1} maximum sampling frequency), which communicates with the control PC via USB. The Anton Paar rheometer is connected via a USB interface to the control tabletop PC where the *RheoCompass* software is run, which controls all the functionalities of the rheometer. The acquisition and analysis of raw signals are performed

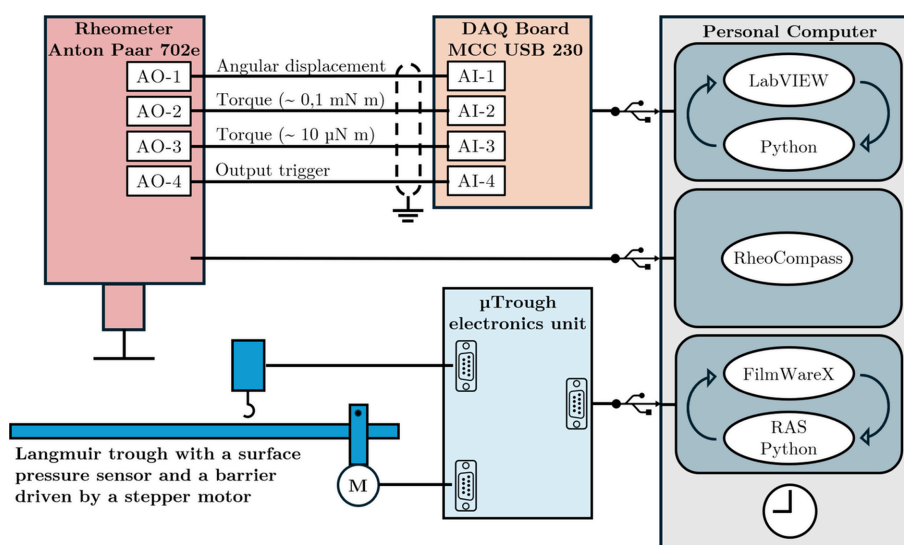


Figure 3 Sketch of the electrical connections. The DAQ board, used to acquire the raw analogue signals from the rheometer, and the control units of the rheometer and Langmuir trough are all connected via USB to a PC running custom-made acquisition/analysis software, rheometer control software and Langmuir trough control software. The interfacial pressure sensor and the barrier motor of the Langmuir trough are connected to their respective control units via serial connections. The four analogue signals from the rheometer are connected to the DAQ board via the analogue input channels using single-ended connections, with all channels sharing the same ground reference.

using custom software developed in *LabVIEW*, which integrates Python subroutines for more complex calculations.

The electromechanics of the Langmuir trough and the interfacial pressure sensor are connected to a Kibron μ Trough measurement and control unit that communicates with the control PC by USB connection. The Kibron proprietary *FilmwareX* software is mounted on the control PC where it is used to operate the trough. In this case, a remote access server (RAS) has been configured that runs along with *FilmwareX*, sharing access to the trough, allowing communication and operation of the trough using string-based commands and responses. This centralized single-PC control allows us to configure our own scripts in Python to automate experiments and/or perform more complex barrier movement profiles at will.

In this work, the synchronization of the rheometry and NR measurements was achieved by ensuring that the time clocks of the rheology and NR systems coincide. In the future, we plan to integrate the Langmuir trough control within *NOMAD*, a software package developed at the ILL, which allows instrument control and data acquisition. This will make it possible to trigger rheology measurements from *NOMAD* or, vice versa, to trigger NR measurements from the rheometer control software, if a very precise synchronization is needed. For the experiments performed so far, this level of synchronization has not been necessary.

2.3. Operation

To operate this experimental setup, four distinct software tools are utilized (i) to control the rheometer, (ii) to acquire the raw torque and angular displacement signals, (iii) to manage the Langmuir trough, and (iv) to operate the neutron reflectometer. In the following, we will describe some peculiarities of each of these functions.

Rheometer control. The correct positioning of the lateral vertices of the ring cross section at the interface level is crucial in this setup. This task can be split into two parts: (i) properly defining the vertical length of the probe fixture and the vertical position of the double wall annular shear channel bottom, which is achieved using *RheoCompass*'s capability of creating user-defined measurement ensembles, and (ii) preparing a vertical positioning script which, starting with the ring above the interface, slowly lowers the probe until a jump in the vertical force measurement is detected. The probe is then lowered another half a millimetre so that the interface pins on the edge of the diamond-shaped cross section of the ring. Finally, the vertical force measurement is reset.

It is necessary to properly configure *RheoCompass* for the intended measurements. The user can define different types of test to conduct oscillatory measurements in a single-frequency mode, frequency sweep mode or amplitude sweep mode. The raw torque, angular displacement and trigger signal are acquired and split into separate waveforms using the trigger signal.

Digitizing raw rheometry signals. A software package has been programmed in *LabVIEW* that performs data acquisition

and splitting of the acquired signal into individual waveforms. For each individual waveform, an integer number of periods is selected, discarding the initial part, which may contain transients. The waveforms $T(t) = T_0^* \exp(i\omega t)$ and $\phi(t) = \phi_0^* \exp(i\omega t)$, where $T_0^* = T_0 \exp(i\varphi_T)$ and $\phi_0^* = \phi_0 \exp(i\varphi_\phi)$, are then processed by discrete Fourier transforms, to obtain the amplitude and phase of both the torque (T_0 , φ_T) and the angular displacement (ϕ_0 , φ_ϕ). From there, the complex amplitude ratio,

$$\begin{aligned} \text{AR}^* &= \frac{T(t)}{\phi(t)} = \frac{T_0^*}{\phi_0^*} = \frac{T_0}{\phi_0} \exp[i(\varphi_T - \varphi_\phi)] \\ &= |\text{AR}^*| \exp[i(\varphi_T - \varphi_\phi)], \end{aligned} \quad (1)$$

is calculated. This serves as input for a purpose-built Python program that implements the corresponding FFBDA scheme and is called from *LabVIEW*, yielding the interfacial dynamic shear moduli by solving the equations that govern the velocity field in both the interface and the bulk. These analysis tasks are performed asynchronously in parallel using a queue system as acquisitions are made.

Langmuir trough management. Kibron components were used in the assembly of the Langmuir trough. Consequently, the Langmuir trough is operated using the company's proprietary software, *FilmwareX*. This software includes a specialized feature that allows the integration of Python scripts, enabling users to employ various operational modes through the RAS on a local network. This capability offers significant flexibility, allowing users to automate the measurement process in coordination with neutron scattering data acquisition. In addition, it facilitates the development of intricate barrier movement profiles, thereby enhancing the precision and complexity of experimental setups.

Operation of the neutron reflectometer. The FIGARO instrument at the ILL is a high-flux time-of-flight (TOF) reflectometer (Campbell *et al.*, 2011). It is equipped with four choppers that allow one to select the wavelength resolution. In this study, for example, it was used with a constant resolution $d\lambda/\lambda = 7\%$. Three different incidence angles $\theta_1 = 0.62^\circ$, $\theta_2 = 1.97^\circ$ and $\theta_3 = 3.8^\circ$ can be configured. Typically, when seeking a measurement that spans a broad wavelength range, it is preferable to measure at angles θ_1 and θ_3 , because their ranges overlap. However, for rapid measurements in studies on kinetic processes (Campbell, 2018), measurements can be made at a single incidence angle tailored to the user's momentum transfer range requirements. The instrument also features the ability to measure surface excess with high precision by measuring at low Q_z (θ_1) on a mixture of heavy and light water with zero neutron reflection (Braun *et al.*, 2017; Campbell, 2018). This makes it possible to quantify the composition of binary mixtures using isotopic contrasts in a suitable manner or in combination with ellipsometry as a complementary technique. On the other hand, when the objective of the study is to obtain information on the evolution of the interfacial structure, it is possible to make measurements using higher incidence angles (θ_2 or θ_3) depending on the range in Q_z where the characteristics of the changes in the

reflectivity curve appear (Carrascosa-Tejedor *et al.*, 2022). Different isotopic contrasts can be tailored to match the structural complexity of the system under study and, using deuteration, distinct components can be selectively highlighted. The two-dimensional detector signal is processed and reduced using *COSMOS* (Gutfreund *et al.*, 2018), ultimately yielding neutron reflectivity R , with respect to the vertical scattering vector Q_z which, considering specular reflection, is defined as follows:

$$Q_z = \frac{4\pi}{\lambda} \sin \theta, \quad (2)$$

where θ is the angle of incidence and λ is the wavelength. Specular NR provides detailed information on layered structures perpendicular to the interface. The experimental data are typically analysed using an optical matrix formalism, in which the reflectivity is calculated for a stack of layers, each characterized by a specific scattering length density (SLD), thickness, roughness and solvent volume fraction. To ensure physical consistency, constraints can be applied within the modelling software. By fitting datasets acquired under different isotopic contrast conditions using a shared structural model, one can determine both the composition and depth profile of the interfacial material with sub-nanometric precision.

2.4. Data analysis

Rheology data analysis. In fluid–fluid interfaces, the contributions of interfacial and bulk phases are intrinsically coupled. Hence, the only way to correctly decouple the two effects is to work with the flow fields at the interface and the bulk fluid phases. Obviously, this makes the task quite complicated compared with analytic calculations. However, several FFBDA schemes have recently been proposed for different ISR configurations, either in longitudinal (Reynaert *et al.*, 2008; Tajuelo *et al.*, 2015; Tajuelo *et al.*, 2016) or in rotational motion (Vandebril *et al.*, 2010; Tajuelo *et al.*, 2017; Sánchez-Puga *et al.*, 2021). In all of them, a simple physical model of the flow geometry allows the user to formulate the Navier–Stokes equations for bulk fluid flows with just one velocity component (in rotational rheometers, such as the DWR, the azimuthal one) (Vandebril *et al.*, 2010; Sanchez-Puga & Rubio, 2025a; Sánchez-Puga & Rubio, 2025b). Then, the stress balance at the interface is included through the Boussinesq–Scriven equation (Reynaert *et al.*, 2008; Vandebril *et al.*, 2010), considering that only shear stresses occur at the interface and in the bulk fluids. The crucial parameter in this problem appears in the Boussinesq–Scriven equation, namely the complex Boussinesq number, Bq^* , which describes the relative importance of the interfacial drag compared with the bulk drag. For the most common case of Newtonian bulk fluid phases and linear viscoelastic interfaces, Bq^* is defined as (Edwards *et al.*, 1991)

$$Bq^* = \frac{\eta_s^*(V/L_s)P_s}{\eta(V/L_b)A_b} \simeq \frac{\eta_s^*}{\eta a}, \quad (3)$$

where η and η_s^* are, respectively, the subphase and complex interfacial viscosities, V is the characteristic velocity, L_s and L_b are characteristic length scales for the decay of linear momentum at the interface and in the bulk fluid, respectively, P_s and A_b are, respectively, the perimeter of the contact line at the probe surface and the area of contact between the probe and the bulk subphase, and a is a length scale defined by the probe’s area-to-perimeter ratio, $a = A_b/P_s$. In the present case, a ring with a diamond cross section with side L , it is usual to consider $a = L$ [for the DWR on the air/water interfaces $L \sim 0.7$ mm (Vandebril *et al.*, 2010; Renggli *et al.*, 2020; Sanchez-Puga & Rubio, 2025a)]. Strictly speaking, L_b and L_s are frequency-dependent scale lengths (Fitzgibbon *et al.*, 2014), so that $Bq^*(\omega) \sim L_b(\omega)/L_s(\omega) \simeq \omega^{-1/4}$. As the typical frequency range in interfacial rheology measurements is not very wide, this dependence can be safely ignored.

When Bq^* is large (say $Bq^* \geq 100$) interfacial stresses dominate and simple expressions (Sánchez-Puga *et al.*, 2021) can be used to obtain the value of Bq^* from the experimental data and, consequently, of η_s^* . Unfortunately, this is not always the case, and then it is necessary to properly analyse the data to separate the contributions of the strongly coupled interfacial and bulk flows.

To that end, an iterative procedure is established that involves (i) solving the Navier–Stokes equations together with the Boussinesq–Scriven equation starting from an initial seed value of Bq^* , (ii) obtaining the values of the interfacial and bulk drags for that flow configuration, and (iii) using the drag values and the experimental value of the complex amplitude ratio, AR^* , to obtain a corrected value for Bq^* through an iterative scheme.

The equation of motion of the DWR can be written as

$$T_0 \exp[i(\omega t + \varphi_T)] + T_s(t) + T_1(t) + T_2(t) = I\ddot{\phi}(t), \quad (4)$$

where the first term is the torque imposed by the motor on the DWR assembly, the next three terms are the torques due to the drag from the interface, bulk phase 1 and bulk phase 2, respectively, and I is the moment of inertia of the rotor and the DWR assembly. Assuming all terms in equation (4) are oscillatory with frequency ω , the time dependence vanishes and we can rewrite the equation of motion as

$$T_0^* + T_{0,s}^* + T_{0,1}^* + T_{0,2}^* = -\omega^2 I \phi_0^*, \quad (5)$$

where the argument of each (complex) term accounts for the phase difference with respect to a given reference. Both T_0^* and ϕ_0^* are measured during the experiment. $T_{0,s}^*$ is proportional to Bq^* , and both $T_{0,1}^*$ and $T_{0,2}^*$ depend on the flow field, which in turn depends on Bq^* . Therefore, Bq^* cannot be directly calculated from the equation of motion and an iterative scheme along the lines previously explained is necessary.

Vandebril *et al.* (2010) first published and made freely available an FFBDA software package (<https://softmat.mat.ethz.ch/opensource.html>) specifically written for DWR interfacial shear rheometer configurations. In the present case, to analyse the data we used a second-generation FFBDA

software package (freely available at <https://github.com/psanchez0046/DWR-Drag> and <https://doi.org/10.5281/zenodo.16459609>) which incorporates the following improvements: (i) a user-selectable increased mesh resolution, (ii) a second-order finite difference approximation for drag calculations, and (iii) an iterative scheme based on the probe's equation of motion. Full details have been published elsewhere (Sanchez-Puga & Rubio, 2025*b*).

Importantly, in the DWR configuration the interfacial strain field can be considered uniform only for high values of Bq^* (say $Bq^* \geq 100$). For lower values of Bq^* , the interfacial strain field is highly non-linear, with the highest strain values just at the probe interface contact line. After convergence, the FFBDA software package can yield the strain value on the contact line. However, for labelling purposes, in the rest of this paper, we will use an average strain value, γ_{av} , obtained from the analytic solution of the Boussinesq–Scriven equation in the limit $Bq^* \rightarrow \infty$. This yields

$$\gamma_{av} = \phi_0 \frac{R_3^2}{R_3^2 - R_6^2} \sim \phi_0 \frac{R_1^2}{R_5^2 - R_1^2}, \quad (6)$$

where ϕ_0 is the amplitude of the angular displacement oscillation and the different radii are as indicated in Fig. 2.

NR data. The measured reflectivity curves (Fig. 6) have been fitted using the *refnx* software (Nelson & Prescott, 2019), which allows modelling of the interfacial structure in terms of several piled-up layers and contains a versatile environment for model refinement and implementation of constraints. For instance, in the case of lipid monolayers, the interface model can be established straightforwardly using a specific macro for the modelling of lipid layers (the ‘LipidLeaflet’ macro). This macro implements the molecular constraint that ensures the same area per molecule (A_{molec}) in both the headgroup layer and the tail layer, in which the lipid monolayer is sub-divided (Gerelli, 2016; Campbell *et al.*, 2018; Nelson & Prescott, 2019). After the fitting procedure, one can obtain an SLD profile across the vertical coordinate and the values of the corresponding parameters defining the transverse structure of the interfacial film (see Table 1).

3. Materials and experimental protocol

The performance of the setup was assessed by measuring Langmuir DPPC monolayers at different interfacial pressures at 22°C. Chain-deuterated DPPC (d_{62} -DPPC) was received from Avanti Polar Lipids (>99% purity). Subphase water, H₂O, was obtained through a Milli-Q dispenser (Millipore) and D₂O was used as received from Sigma–Aldrich. The Langmuir trough, the annular shear channel and the lateral barrier were meticulously cleaned with chloroform (Sigma–Aldrich). All of these components were carefully rinsed with water to remove any remaining residues. The DWR probe was submerged in chloroform about 5 min before each experiment for cleaning.

The chloroform solutions of the lipids were prepared at concentration 0.5 mg ml⁻¹ and gently spread dropwise on the

interface using a Hamilton micro-syringe until the interfacial pressure was approximately 2–3 mN m⁻¹. The chloroform was then allowed to evaporate and the monolayer left to equilibrate for 15 min. Sequential increases in interfacial pressure, using the constant-pressure mode of operation between steps, allowed at each step the acquisition of full Q_z range NR measurements simultaneously with a set of continuous rheological measurements at a single frequency (3% strain and 0.5 Hz), followed by measurements during a frequency sweep (0.3–3 Hz at 3% strain) and a strain sweep (1–10% at frequency 0.5 Hz).

Finally, all the measurements shown in this paper have been performed in strain-controlled mode (TruStrain) to avoid excessive strains that could extremely shear the sample. However, in the rotational rheometer used here, this strain-control mode is implemented through a rather fast feedback loop which governs the electromechanical torque imposed on the probe+rotor ensemble.

4. Experimental validation of instrument performance

Simultaneous NR and ISR measurements were carried out on DPPC monolayers at constant interfacial pressure to test the performance of the experimental setup. DPPC is one of the most studied phospholipids, so there exists an extensive literature using neutron reflectivity (Campbell *et al.*, 2018; Carrascosa-Tejedor *et al.*, 2020) and ISR (Kim *et al.*, 2011; Hermans & Vermant, 2014) with which to compare our measurements. Deuterated DPPC was used, with air contrast matched water (ACMW, a mixture of 8.2% D₂O and 91.8% H₂O leading to an SLD = 0 that matches the air layer) and pure subphases of D₂O subphases. Measurements have been made at relatively high interfacial pressures (25, 35 and 45 mN m⁻¹) away from the liquid expanded to liquid condensed (LE–LC) phase transition (about 8 mN m⁻¹) (Campbell *et al.*, 2018), but still yielding loss modulus $G''_s(\omega)$ values low enough to show the instrument's resolution limit.

Validation of the DWR ISR. In panels (a) and (c) of Fig. 4 we show the frequency dependence (where f is the frequency in Hz) of the modulus of the complex amplitude ratio, $|AR^*(f)|$ [panel (a)], and the phase lag between the torque and the angular displacement signals, $\varphi(f)$ [panel (c)], on the oscillation frequency, at the same interfacial strain $\gamma_s = 3\%$. The data belong to a clean air/water interface and DPPC monolayers on two subphases, with different NR contrasts (ACMW and D₂O, respectively), at three different interfacial pressures: $\Pi = 25$ (red), 35 (green) and 45 (blue) mN m⁻¹. The uncertainty in all the interfacial rheology data shown here has been estimated as indicated in Section 1 of the supporting information.

The values of the modulus of the amplitude ratio, $|AR^*(f)|$, show similar trends for all the investigated interfaces and are practically indistinguishable in the logarithmic representation. Moreover, the values of the modulus of the amplitude ratio show a clear trend with f^2 that indicates that the system is working in a regime where the effects due to the inertia of the rotor+probe ensemble are relevant. Furthermore, the phase

lag graphs between the applied torque and the angular displacement, $\varphi(f)$, show in all cases smooth low-noise curves with values close to π rad, as expected when the rotor+probe inertia is important. For this geometry and the frequency range explored here, the two most important contributions to AR^* are the interfacial effects and the inertia of the instrument. Interestingly, the $\varphi(f)$ curves approach each other at high frequency and apparently show a decreasing trend above a frequency that depends on the specific interfacial system (surfactant and bulk fluid phases). In any case, data for $f \gtrsim 1$ Hz should be considered with some reservation.

In panels (b) and (d) of Fig. 4 we show the dependence of the modulus of the complex amplitude ratio, $|AR^*|$ [panel (b)], and the phase delay between the torque and angular displacement signals, φ [panel (d)], on the interfacial strain, γ_s , at a constant frequency, $f = 0.5$ Hz. Again, the data correspond to a clean air/water interface and DPPC monolayers on two subphases, with different NR contrasts (ACMW and D_2O , respectively), at three different interfacial pressures: $\Pi = 25$ (red), 35 (green) and 45 (blue) $mN m^{-1}$. The limited amount

of time allocated at the ILL for these experiments did not allow measurement of the strain sweep in the DPPC on the ACMW subphase at $\Pi = 25 mN m^{-1}$. Note that the error bars are smaller than the symbols.

The measured values for $|AR^*|$ or φ show a very small dependence on the strain. Notice that, in contrast to Fig. 4(a), here the vertical axis scale is linear, and all the values represented here differ by less than 4%. The data in Fig. 4(b) corresponding to the interfaces with a stronger rheological response (DPPC at 45 $mN m^{-1}$) show smaller $|AR^*|$ than those corresponding to a clean interface, which can seem counterintuitive considering that AR^* is defined as T_0^*/ϕ_0^* (the more rheologically responsive DPPC at the $\Pi = 45 mN m^{-1}$ interface seems to require a lower torque to be sheared than that corresponding to a clean interface). However, a viscoelastic interface in an oscillatory experiment can give rise to a resonant response. In the high Bq^* regime, equation (4) can be approximated as

$$T_0 \exp[i(\omega t + \varphi_T)] + T_s(t) = I\ddot{\phi}(t), \quad (7)$$

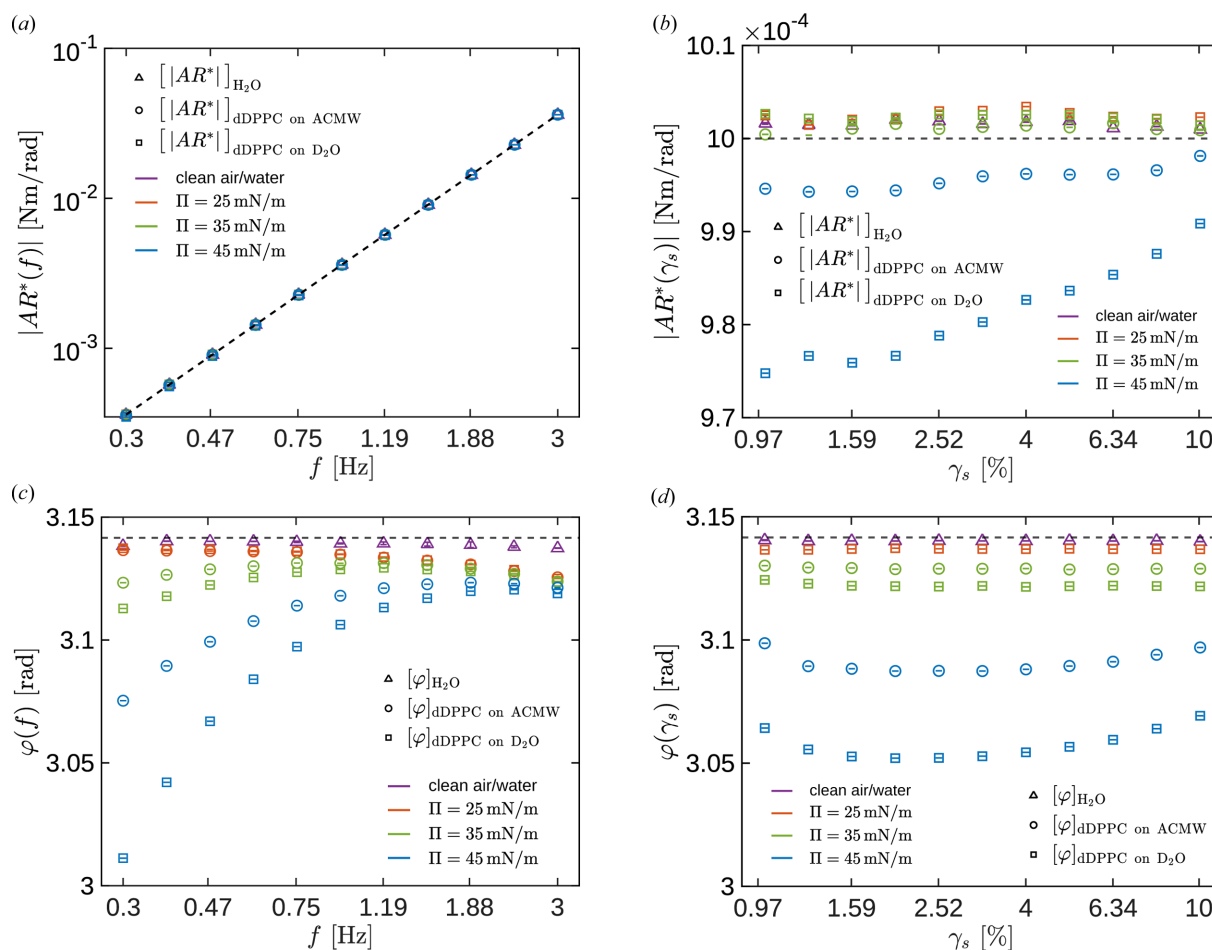


Figure 4 (a) $|AR^*(f)|$ at $\gamma = 3\%$. (b) $|AR^*(\gamma_s)|$ at $f = 0.5$ Hz. (c) $\varphi(f)$ at $\gamma = 3\%$. (d) $\varphi(\gamma_s)$ at $f = 0.5$ Hz. DPPC monolayers on ACMW (circles) and D_2O (squares) subphases, at $\Pi = 25 mN m^{-1}$ (red), $\Pi = 35 mN m^{-1}$ (green) and $\Pi = 45 mN m^{-1}$ (blue). The clean air/water interface is represented with purple triangles. A dashed line with slope 2 in panel (a), a dashed horizontal line at 10^{-3} in panel (c), and a dashed horizontal line at π in panels (b) and (d) have been plotted to guide the eye.

where the torque resulting from the drag from the interface is proportional to $-\eta_s^* \dot{\phi}(t)$,

$$T_s(t) = -i\omega C_g \eta_s^* \phi_0 \exp[i(\omega t + \varphi_\phi)],$$

C_g being a positive geometric coefficient (Renggli *et al.*, 2020; Sánchez-Puga *et al.*, 2021). From equation (7) and considering $\eta_s^* = \eta_s' - i\eta_s''$, the amplitude ratio is given by

$$\text{AR}^* = i\omega \eta_s' C_g + \omega \eta_s'' C_g - I\omega^2, \quad (8)$$

so that its modulus is

$$|\text{AR}^*| = \sqrt{(\omega \eta_s'' C_g - I\omega^2)^2 + (\omega \eta_s' C_g)^2}. \quad (9)$$

From equation (9) it is now apparent that, in a system where the governing contributions are the inertia and the interfacial drag, $|\text{AR}^*|$ shows a minimum when the interfacial storage modulus is such that $\omega \eta_s'' C_g - I\omega^2 = 0$ (a detailed description of the corresponding second-order dynamic model is provided in Section 2 of the supporting information). Therefore, the raw data shown in Fig. 4(b) suggest, prior to any data analysis, that the DPPC interfaces at 45 mN m^{-1} must have a measurable

storage modulus and, furthermore, that its value must change with strain amplitude.

The loss and storage modulus corresponding to the measurements shown in Fig. 4 are shown in Fig. 5, where the dotted lines labelled ‘inertia’ indicate that below that line the inertia of the rotor+probe dominates and limits the operational window of the instrument (Renggli *et al.*, 2020). In other words, the dotted lines represent the conditions in which the dynamic modulus values (G_s' or G_s'') are equal to

$$\frac{I\omega^2}{C_\Phi/C_M}, \quad (10)$$

where C_Φ/C_M is a geometric coefficient (Renggli *et al.*, 2020; Sánchez-Puga *et al.*, 2021), that is,

$$\frac{C_\Phi}{C_M} = 4\pi \left(\frac{R_5^2 R_1^2}{R_5^2 - R_1^2} + \frac{R_6^2 R_3^2}{R_3^2 - R_6^2} \right). \quad (11)$$

In the plots of the storage modulus, Figs. 5(c) and 5(d), the inertia lines are too close to most of the G_s' data, apart from those at $\Pi = 45 \text{ mN m}^{-1}$. Hence, probably only the values of

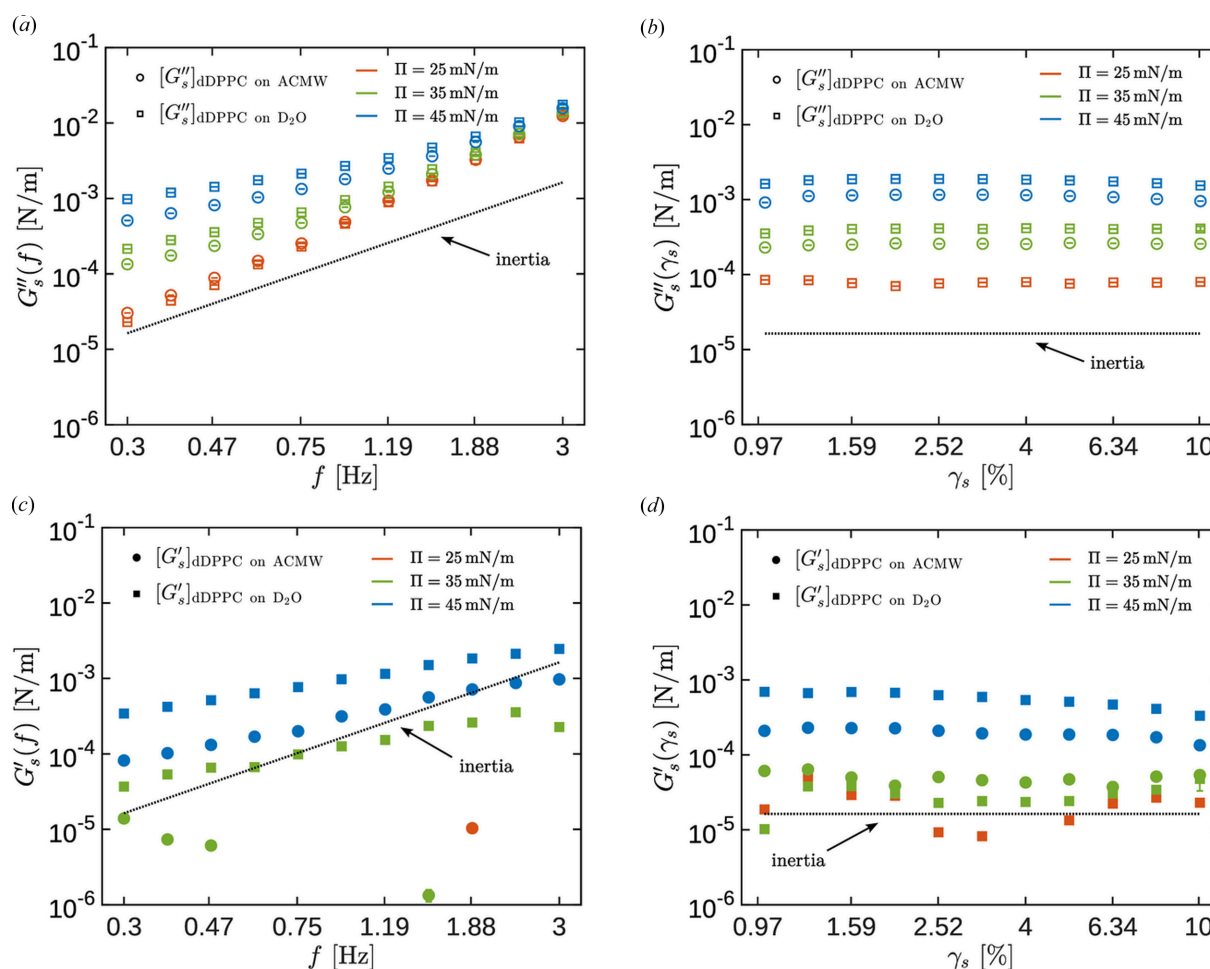


Figure 5

(a) Loss modulus $G_s''(f)$ at $\gamma_s = 3\%$. (b) Loss modulus $G_s''(\gamma_s)$ at $f = 0.5 \text{ Hz}$. (c) Storage modulus $G_s'(f)$ at $\gamma_s = 3\%$. (d) Storage modulus $G_s'(\gamma_s)$ at $f = 0.5 \text{ Hz}$. DPPC monolayers onto ACMW (circles) and D₂O (squares) subphases, at $\Pi = 25 \text{ mN m}^{-1}$ (red), $\Pi = 35 \text{ mN m}^{-1}$ (green) and $\Pi = 45 \text{ mN m}^{-1}$ (blue). The dotted line indicates the inertia-limited sensitivity.

the storage modulus measured here at $\Pi = 45 \text{ mN m}^{-1}$ are reliable.

Regarding the frequency dependence in Figs. 5(a) and 5(c), typically, the calculated values of the storage modulus, $G'_s(f)$, are smaller than those of the loss modulus, $G''_s(f)$, under the same conditions of subphase, interfacial pressure, frequency and strain. In Fig. 5(a) most data, except perhaps those at $\Pi = 25 \text{ mN m}^{-1}$ and the lower frequencies, are far enough from the inertia limit. However, in Fig. 5(c) only the $G'_s(f)$ data corresponding to $\Pi = 45 \text{ mN m}^{-1}$ appear to be far enough from the inertia limit to be considered reliable. At 45 mN m^{-1} the elastic component $G'_s(f)$ is smaller than the viscous one $G''_s(f)$, but becomes significant, approaching the same order of magnitude as the viscous component.

Several other aspects of the frequency dependence of the loss modulus [see Fig. 5(a)] can be observed. First, the loss modulus increases with the interfacial pressure, as expected. Second, the monolayers on a D_2O subphase show loss modulus values systematically higher than those of the monolayers loaded on ACMW subphases. Third, all curves converge at high frequency, as expected from the curves shown in panels (a) and (c) of Fig. 4.

Regarding the dependence of strain amplitude (at $f = 0.5 \text{ Hz}$), shown in panels (b) and (d) of Fig. 5, the loss modulus is in all cases above the inertia limit and is fairly constant for all strain amplitude values within the explored range (1–10%) and any of the interfacial pressures reported. Moreover, panels (b) and (d) of Fig. 5 show that for 35 and 45 mN m^{-1} interfacial pressure $G'_s(\gamma)$ is consistently higher than $G''_s(\gamma)$, confirming the viscosity-dominated character of the monolayer. Therefore, the strain amplitude value used in the frequency sweeps ($\gamma_s = 3\%$) can be safely assumed to lie within the material's linear regime with the current experimental configuration and for the DPPC monolayers investigated in this study. Measurements at strains below 1% are not technically feasible due to the inertia of the motor drive, which represents a limiting factor in interfacial rheometry. The storage modulus for the weaker interfaces ($\Pi = 25$ and 35 mN m^{-1}) is closer to the inertia limit, which means that the elastic response of these interfaces is close to the instrument sensitivity. For the more responsive interfaces ($\Pi = 45 \text{ mN m}^{-1}$), G'_s is well above the inertia limit and a slight decrease can be observed for γ_s above 4%, in good agreement with the previous analysis of the raw $|\text{AR}^*|$ data.

From a physical perspective, at such a high interfacial pressure the monolayer is expected to be in the LC phase. Although the lateral diffusion of phospholipid molecules is significantly reduced compared with the LE phase, the system still appears to retain a fluid character, with some molecular motion and dissipative processes remaining possible. Such lateral mobility should be higher at lower interfacial pressures and, therefore, the storage modulus would be expected to decrease faster than the loss modulus upon decreasing the interfacial pressure. Such a tendency is confirmed by the strain dependence measurements shown in Figs. 5(b) and 5(d). Hence, it is not surprising that, at the interfacial dynamical conditions used here, the interface exhibits a predominantly

Table 1

Summary table with the two-layer model parameters at different interfacial pressures.

Parameter	$\Pi = 25 \text{ mN m}^{-1}$	$\Pi = 35 \text{ mN m}^{-1}$	$\Pi = 45 \text{ mN m}^{-1}$
V_{AC}^\dagger	759 \AA^3	759 \AA^3	759 \AA^3
V_{PC}^\dagger	344 \AA^3	344 \AA^3	344 \AA^3
t_{AC}	$(16.27 \pm 0.01) \text{ \AA}$	$(17.09 \pm 0.01) \text{ \AA}$	$(17.41 \pm 0.01) \text{ \AA}$
t_{PC}^\dagger	9 \AA	9 \AA	9 \AA
σ^\dagger	3.45 \AA	3.88 \AA	4.53 \AA
$A_{\text{molec}}^\ddagger$	$(46.66 \pm 0.02) \text{ \AA}^2$	$(44.42 \pm 0.02) \text{ \AA}^2$	$(43.60 \pm 0.02) \text{ \AA}^2$
$\phi_{\text{PC,w}}$	$(18 \pm 0.03)\%$	$(14 \pm 0.03)\%$	$(12 \pm 0.04)\%$
$\text{SLD}_{\text{D}_2\text{O}}^\ddagger$	$(5.812 \pm 0.002) \text{ \AA}^{-2}$	$(5.771 \pm 0.003) \text{ \AA}^{-2}$	$(5.660 \pm 0.002) \text{ \AA}^{-2}$
$(\times 10^{-6})$			
$\text{SLD}_{\text{PC}}^\dagger$	1.74 \AA^{-2}	1.74 \AA^{-2}	1.74 \AA^{-2}
$(\times 10^{-6})$			
$\text{SLD}_{\text{AC}}^\dagger$	8.08 \AA^{-2}	8.08 \AA^{-2}	8.08 \AA^{-2}
$(\times 10^{-6})$			
χ^2	26.7	36.2	15.83

[†] Parameters taken from the literature (Campbell *et al.*, 2018; Ocko *et al.*, 1994). [‡] Treated as a free parameter in the fitting procedure.

viscous behaviour. Such behaviour is also consistent with previous reports in the literature. For instance, Espinosa *et al.* (2011) and Kim *et al.* (2011, 2013) have shown that DPPC monolayers in condensed phases exhibit fluid-like behaviour. More recently, Hermans & Vermant (2014) described DPPC interfaces as dominated by viscous behaviour, for the same pressure, frequency and temperature ranges studied here.

Simultaneous neutron reflectometry measurements. The data for the two isotropic contrasts were co-refined under the assumption that the chemical structures are identical in both cases. The thickness of the acyl chains (AC) is $t_{\text{AC}} = V_{\text{AC}}/A_{\text{molec}}$, as we assume full occupancy of the tail group, and the thickness of the phosphatidylcholine (PC) headgroup is $t_{\text{PC}} = V_{\text{PC}}/[A_{\text{molec}}(1 - \phi_{\text{PC,w}})]$, where $\phi_{\text{PC,w}}$ is the hydration fraction of the headgroup.

The values of the parameters used in the two-layer model are shown in Table 1. The background for the ACMW contrast was fixed at 5×10^{-6} , and for the D_2O contrast at 10^{-7} . The molecular volume of the acyl chain was fixed to that corresponding to the LC phase ($V_{\text{AC}} = 759 \text{ \AA}^3$), the molecular volume of the PC headgroup was fixed to $V_{\text{PC}} = 344 \text{ \AA}^3$ and the thickness of the headgroup was fixed to 9 \AA , all taken from Campbell *et al.* (2018). The interfacial roughness (σ) was fixed to the value corresponding to the capillary waves according to Ocko *et al.* (1994). The modest increase in interfacial roughness from 3.45 to 4.53 \AA upon compression may signal the onset of out-of-plane fluctuations or molecular protrusions as the monolayer approaches its collapse pressure.

The SLD of D_2O , $\text{SLD}_{\text{D}_2\text{O}}$, was treated as a free parameter and shows decreasing values due to exchange with atmospheric water. The observed progressive increase in acyl chain thickness from 16.27 to 17.41 \AA upon compression from 25 to 45 mN m^{-1} indicates a slight chain extension and vertical orientation. The modest magnitude of this change, despite a $\sim 7\%$ reduction in area per molecule, suggests that the chains are already well oriented at 25 mN m^{-1} and that further compression primarily reduces lateral packing defects rather than driving additional chain ordering. The long acquisition times needed for the NR measurements preclude

the possibility of making continuous isothermal compressions. However, the fitted molecular areas are in good agreement with previous reference continuous isotherms of hydrogenous and deuterated DPPC monolayers [see, for instance, Fig. 5(a) of Campbell *et al.* (2018)]. In general, the two-layer model parameters obtained are in good agreement with those previously reported from independent FIGARO measurements (Campbell *et al.*, 2018; Carrascosa-Tejedor *et al.*, 2020).

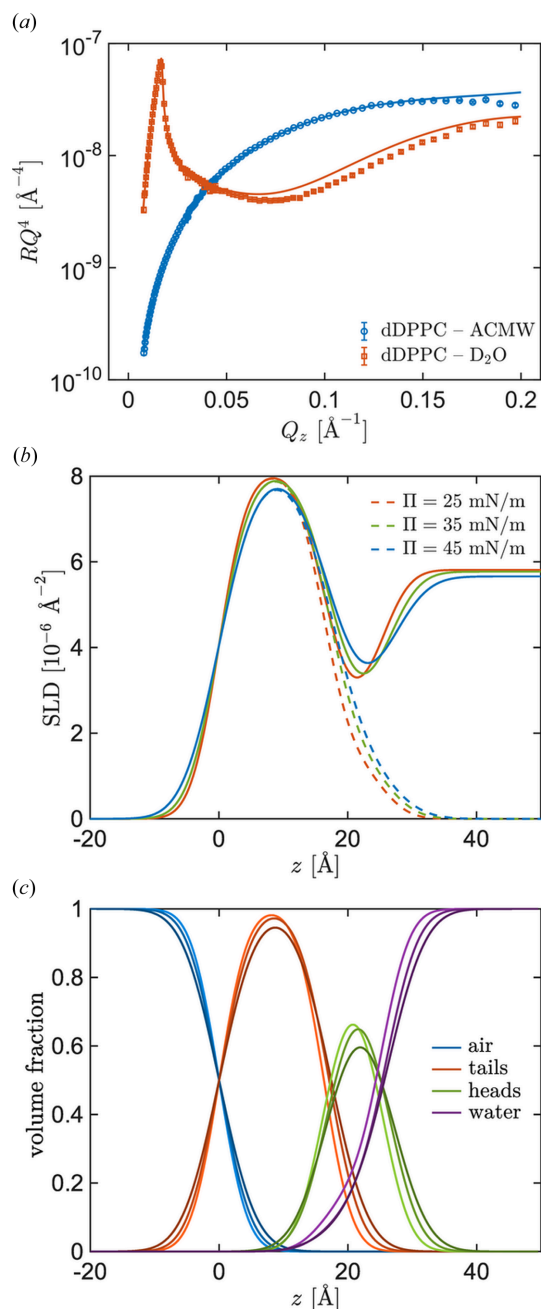


Figure 6
(a) RQ^4 , as a function of the vertical scattering vector, Q_z , at $\Pi = 25 \text{ mN m}^{-1}$ for the two different subphases used here. (b) Calculated SLD profiles at $\Pi = 25 \text{ mN m}^{-1}$ (red lines), $\Pi = 35 \text{ mN m}^{-1}$ (green lines) and $\Pi = 45 \text{ mN m}^{-1}$ (blue lines); dashed lines: ACMW subphase; continuous lines: D_2O subphase. (c) Volume fraction profiles of different slabs: air (blue), tails (red), heads (green) and water (purple). Lighter traces correspond to lower interfacial pressure.

In Fig. 6 we show illustrative examples of the data obtained through the NR measurements. Fig. 6(a) shows an example of the reflectivity curves at $\Pi = 25 \text{ mN m}^{-1}$ for the two measured contrasts (see the supporting information for the corresponding curves at $\Pi = 35$ and 45 mN m^{-1}). Figs. 6(b) and 6(c) display, respectively, the calculated SLD profiles with the different contrasts (subphases) at different interfacial pressures and the corresponding volume fraction of the defined slabs in the vertical coordinate at different interfacial pressures. The origin of the vertical coordinate, z , is set at the air–tails dividing surface.

The fit of the reflectivity curve corresponding to the interfacial pressure of 25 mN m^{-1} is shown in Fig. 6(a). The corresponding SLD profile and the volume fraction representation [Figs. 6(b) and 6(c)] at different interfacial pressures reveal systematic trends with increasing interfacial pressure which can be correlated to the values reported in Table 1: (i) the peak and valley positions, corresponding to the tail and head regions, respectively, shift upwards owing to the slight increase in tail thickness, and (ii) the SLD in the head region increases due to a decrease in the water volume fraction. This trend reflects changes in the hydration of the lipid headgroup: as the interfacial pressure increases, the water content in the headgroup decreases, leading to a higher SLD. The systematic decrease in headgroup hydration upon compression from 18% at 25 mN m^{-1} to 12% at 45 mN m^{-1} water volume fraction reflects progressive dehydration of the phosphatidylcholine moieties as intermolecular spacing decreases. Importantly, the persistence of $\sim 12\%$ water even at the highest pressure indicates that the headgroups retain a hydration shell that enables molecular rearrangement under shear. This residual hydration is consistent with the predominantly viscous rheological response ($G_s'' > G_s'$) observed, as complete dehydration would be expected to yield a more elastic, solid-like behaviour characteristic of a true solid phase.

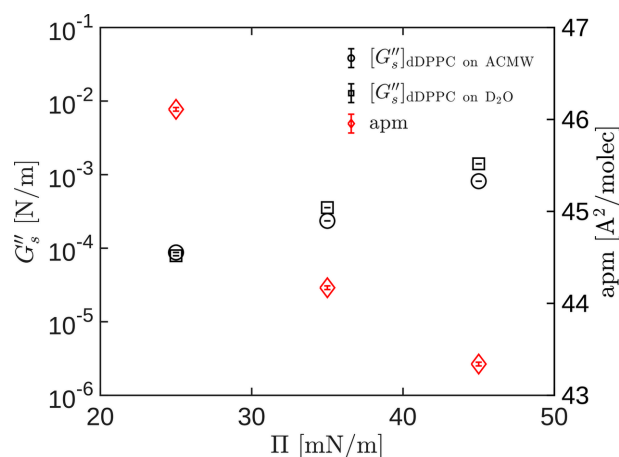


Figure 7
Simultaneous measurements of the loss modulus (left axis; black symbols), G_s'' , and the area per molecule (right axis, red diamonds) at $f = 0.5 \text{ Hz}$ and $\gamma_s = 3\%$, at three interfacial pressure values. Circles and squares correspond to DPPC monolayers onto ACMW and D_2O subphases, respectively.

Finally, we put together the information obtained from the simultaneous measurement of interfacial rheology and neutron reflectometry, with ACMW and D₂O subphases. In Fig. 7, we show the graphs of the loss modulus G''_s (left axis, black symbols) and the area per molecule A_{molec} (right axis, red symbols) as a function of interfacial pressure. All rheological measurements were taken at $f = 0.5$ Hz and $\gamma_s = 3\%$, at three interfacial pressure values. The values shown are the averages of at least 20 measurements, and the error bars represent the standard error of the mean. The circles and squares refer to the DPPC monolayers on the ACMW and D₂O subphases, respectively. For DPPC monolayers, an exponential relationship between the loss modulus and the interfacial pressure can be observed (see Fig. 7). The measured values of the dynamic moduli agree well with previous studies (Kim *et al.*, 2011; Kim *et al.*, 2013; Hermans & Vermant, 2014). Moreover, the dependencies of G''_s and A_{molec} on interfacial pressure are consistent with each other: the higher the interfacial pressure, the higher the dynamic moduli, and the lower the mean area available for the surfactant molecules. This is expected since the higher the interfacial pressure, the more compact the molecules are, and their mobility is reduced. In any case, Figs. 6 and 7 show no evidence of multilayer formation within the duration of the experiment. This is not surprising since the spreading pressure of the DPPC monolayers is about 45 mN m^{-1} (Mansour & Zografis, 2007; Hermans & Vermant, 2014). This conclusion cannot be obtained from the pressure–area isotherm alone.

5. Related literature

The following references are cited in the supporting information: Kay (1993), Klein *et al.* (2019), Singh *et al.* (2019), Stoica & Moses (2005).

6. Conclusions

We describe a new sample environment setup that allows one to perform *in situ* simultaneous measurements of neutron reflectivity and interfacial rheology on the same sample. A rotational rheometer with DWR geometry has been coupled to a Langmuir trough that fits on the FIGARO anti-vibration table. An *ad hoc* data acquisition programme has been developed to obtain and analyse torque and angular position signals that allow the calculation of interfacial dynamic moduli on the fly. Hence, the viscoelastic properties of fluid interfaces can be measured simultaneously with neutron reflectometry data. This combined facility allows studies on the interrelation between the microscopic structure and the mechanics of interfacial systems.

We validated the performance of the full system by simultaneously studying the structural and rheological properties of DPPC monolayers at the air/water interface. Different aqueous subphases that yield different contrasts for NR have been used. The rheological behaviour of the samples has been studied by oscillatory measurements under frequency and strain sweeps. The NR results have been satisfactorily

analysed with a simple monolayer model. The results yielded by simultaneous measurements using both interfacial shear rheometry and neutron reflectometry techniques agree well with previous results available in the literature. Collectively, the observed structural trends establish a direct molecular-scale foundation for the macroscopic rheological response: as the monolayer compresses, reduced molecular mobility and altered headgroup hydration lead to higher interfacial shear dynamic moduli.

The combination of instrumental techniques proposed here is especially suitable for studies such as (i) clarifying whether changes in the interfacial rheological properties are due to multilayer formation or not, (ii) correlating the changes of dynamical and structural parameters in kinetic processes (adsorption, diffusion *etc.*), (iii) characterization of monolayer phase transitions, including thermodynamic, mechanical and structural aspects, and (iv) studies on interfacial systems where the molecules are not available in a deuterated version but show strong changes in their interfacial rheological properties: polymers, proteins/peptides in biological membranes *etc.* This setup is essential to determine whether the data collected during a full- Q measurement (typically 1 h duration: 5–15 min at θ_1 and 25–50 min at θ_2) correspond to a steady, transient or out-of-equilibrium state. As a bonus, this combination of techniques is economical with respect to experimental materials, which is of great interest when dealing with particularly expensive or precious samples.

Acknowledgements

The authors gratefully acknowledge Simon Wood for his support with mechanical design and fabrication, and the Partnership for Soft Condensed Matter (PSCM) for access to its laboratories. We acknowledge the beamtime allocation on FIGARO (<https://doi.ill.fr/10.5291/ILL-DATA.9-12-725>, <https://doi.ill.fr/10.5291/ILL-DATA.9-12-726>, <https://doi.ill.fr/10.5291/ILL-DATA.9-13-1089>).

Conflict of interest

The authors have no conflict of interest to disclose.

Data availability

NR data supporting the findings of this study are available from the ILL Data Portal (<https://doi.ill.fr/10.5291/ILL-DATA.9-12-725>, <https://doi.ill.fr/10.5291/ILL-DATA.9-12-726>, <https://doi.ill.fr/10.5291/ILL-DATA.9-13-1089>). Data will be publicly available after the standard 3-year embargo period. ISR and Langmuir data are available from the corresponding author upon reasonable request.

Funding information

This work was supported by the Spanish Ministerio de Ciencia e Innovación (MCIN) – Agencia Estatal de Investigación (MCIN/AEI/10.13039/501100011033) through projects PID2020-

117080RB-C54 and PID2023-147948OB-C33 (JT and MAR). AM was supported by PID2021-129054NA-I00 funded by MICIU/AEI/10.13039/501100011033 and FEDER, UE; by the Department of Education of the Basque Government under grant PIBA-2023-1-0054; and by the IKUR Strategy project IKUR-Neutrónica 2025-2026 (NEU6.NANOBIO). PSP acknowledges the MICINN-ILL postdoctoral program for supporting his stay at the ILL.

References

- Alicke, A., Stricker, L. & Vermant, J. (2023). *J. Colloid Interface Sci.* **652**, 317–328.
- Ashkenazi, D., Pham, K., Vermant, J., Wagner, N. J. & Gottlieb, M. (2024). *J. Rheol.* **68**, 785–799.
- Barman, S. & Christopher, G. F. (2016). *J. Rheol.* **60**, 35–45.
- Beltramo, P. J. & Vermant, J. (2016). *ACS Omega* **1**, 363–370.
- Braun, L., Uhlig, M., von Klitzing, R. & Campbell, R. A. (2017). *Adv. Colloid Interface Sci.* **247**, 130–148.
- Brooks, C. F., Fuller, G. G., Frank, C. W. & Robertson, C. R. (1999). *Langmuir* **15**, 2450–2459.
- Campbell, R. A. (2018). *Curr. Opin. Colloid Interface Sci.* **37**, 49–60.
- Campbell, R. A., Saaka, Y., Shao, Y., Gerelli, Y., Cubitt, R., Nazaruk, E., Matyszewska, D. & Lawrence, M. J. (2018). *J. Colloid Interface Sci.* **531**, 98–108.
- Campbell, R. A., Wacklin, H. P., Sutton, I., Cubitt, R. & Fragneto, G. (2011). *Eur. Phys. J. Plus* **126**, 107.
- Carrascosa-Tejedor, J., Miñarro, L. M., Efstratiou, M., Varga, I., Skoda, M. W. A., Gutfreund, P., Maestro, A., Lawrence, M. J. & Campbell, R. A. (2023). *Nanoscale* **15**, 11141–11154.
- Carrascosa-Tejedor, J., Santamaria, A., Pereira, D. & Maestro, A. (2020). *Coatings* **10**, 507.
- Carrascosa-Tejedor, J., Santamaria, A., Tummino, A., Varga, I., Efstratiou, M., Lawrence, M. J., Maestro, A. & Campbell, R. A. (2022). *Chem. Commun.* **58**, 10687–10690.
- Collada, A., Carrascosa-Tejedor, J., Sánchez-Puga, P., Liguori, A., Gutfreund, P., Santamaria, A., Castillo-Sánchez, J. C., Maestro, A., Cruz, A. & Pérez-Gil, J. (2026). *J. Colloid Interface Sci.* **701**, 138769.
- Daillant, J. & Gibaud, A. (2008). *X-ray and Neutron Reflectivity: Principles and Applications*, Vol. 770. Springer.
- Ducharme, D., Tessier, A. & Russev, S. C. (2001). *Langmuir* **17**, 7529–7534.
- Edwards, D. A., Brenner, H., Wasan, D. T. & Kraynik, A. M. (1991). *Interfacial Transport Processes and Rheology*. Butterworth-Heinemann.
- Erni, P., Fischer, P., Windhab, E. J., Kusnezov, V., Stettin, H. & Läger, J. (2003). *Rev. Sci. Instrum.* **74**, 4916–4924.
- Espinosa, G., López-Montero, I., Monroy, F. & Langevin, D. (2011). *Proc. Natl Acad. Sci. USA* **108**, 6008–6013.
- Fitzgibbon, S., Shaqfeh, E. S. G., Fuller, G. G. & Walker, T. W. (2014). *J. Rheol.* **58**, 999–1038.
- Fuller, G. G. & Vermant, J. (2012). *Annu. Rev. Chem. Biomol. Eng.* **3**, 519–543.
- Gerber, F., Krafft, M. P., Vandamme, T. F., Goldmann, M. & Fontaine, P. (2006). *Biophys. J.* **90**, 3184–3192.
- Gerelli, Y. (2016). *J. Appl. Cryst.* **49**, 330–339.
- Gonzalez-Martinez, J. F., Kakar, E., Erkselius, S., Rehnberg, N. & Sotres, J. (2019a). *Langmuir* **35**, 6015–6023.
- Gonzalez-Martinez, J. F., Kakar, E., Erkselius, S., Rehnberg, N. & Sotres, J. (2019b). *Wear* **418–419**, 151–159.
- Gutfreund, P., Saerbeck, T., Gonzalez, M. A., Pellegrini, E., Laver, M., Dewhurst, C. & Cubitt, R. (2018). *J. Appl. Cryst.* **51**, 606–615.
- Guzmán, E., Llamas, S., Maestro, A., Fernández-Peña, L., Akanno, A., Miller, R., Ortega, F. & Rubio, R. G. (2016). *Adv. Colloid Interface Sci.* **233**, 38–64.
- Guzmán, E., Martínez-Pedrero, F., Calero, C., Maestro, A., Ortega, F. & Rubio, R. G. (2022). *Adv. Colloid Interface Sci.* **302**, 102620.
- Hermans, E. & Vermant, J. (2014). *Soft Matter* **10**, 175–186.
- Huang, Y.-H. & Frostad, J. M. (2025). *Soft Matter* **21**, 6207–6219.
- Kaganer, V. M., Möhwald, H. & Dutta, P. (1999). *Rev. Mod. Phys.* **71**, 779–819.
- Kale, S. K., Cope, A. J., Goggin, D. M. & Samaniuk, J. R. (2021). *J. Colloid Interface Sci.* **582**, 1085–1098.
- Kay, S. M. (1993). *Fundamentals of Statistical Signal Processing: Estimation Theory*. Prentice-Hall.
- Keim, N. C. & Arratia, P. E. (2013). *Soft Matter* **9**, 6222.
- Kim, K., Choi, S. Q., Zasadzinski, J. A. & Squires, T. M. (2011). *Soft Matter* **7**, 7782.
- Kim, K. H., Choi, I. Q., Zell, Z. A., Squires, T. M. & Zasadzinski, J. A. (2013). *Proc. Natl Acad. Sci. USA* **110**, E3054–E3060.
- Klein, C. O., Theodoratou, A., Rühs, P. A., Jonas, U., Loppinet, B., Wilhelm, M., Fischer, P., Vermant, J. & Vlassopoulos, D. (2019). *Rheol. Acta* **58**, 29–45.
- Krafft, M. P., Giulieri, F., Fontaine, P. & Goldmann, M. (2001). *Langmuir* **17**, 6577–6584.
- López-Díaz, D., Merchán, M. D., Velázquez, M. M. & Maestro, A. (2020). *Appl. Mater. Interfaces* **12**, 25453–25463.
- Lu, J., Thomas, R. & Penfold, J. (2000). *Adv. Colloid Interface Sci.* **84**, 143–304.
- Maestro, A. (2019). *Curr. Opin. Colloid Interface Sci.* **39**, 232–250.
- Maestro, A., Deshmukh, O. S., Mugele, F. & Langevin, D. (2015). *Langmuir* **31**, 6289–6297.
- Maestro, A. & Gutfreund, P. (2021). *Adv. Colloid Interface Sci.* **293**, 102434.
- Maestro, A., Jones, D., Sánchez de Rojas Candela, C., Guzman, E., Duits, M. H. & Cicuta, P. (2018). *Langmuir* **34**, 7067–7076.
- Maestro, A., Rio, E., Drenckhan, W., Langevin, D. & Salonen, A. (2014). *Soft Matter* **10**, 6975–6983.
- Mansour, H. M. & Zografi, G. (2007). *Langmuir* **23**, 3809–3819.
- Nelson, A. R. J. & Prescott, S. W. (2019). *J. Appl. Cryst.* **52**, 193–200.
- Nestler, P. & Helm, C. A. (2017). *Opt. Express* **25**, 27077–27085.
- Novaes-Silva, M. C., Rodríguez-Hakim, M., Collada, A., Thompson, B. R., Sanchez-Puga, P., Pham, K., Tajuelo, J., Gutfreund, P., Pérez-Gil, J., Rubio, M. A., Wagner, N. J. & Vermant, J. (2025). *Soft Matter* **21**, 7963–7973.
- Ocko, B. M., Wu, X. Z., Sirota, E. B., Sinha, S. K. & Deutsch, M. (1994). *Phys. Rev. Lett.* **72**, 242–245.
- Pepicelli, M., Verwijlen, T., Tervoort, T. A. & Vermant, J. (2017). *Soft Matter* **13**, 5977–5990.
- Petkov, J. T., Gurkov, T. D., Campbell, B. E. & Borwankar, R. P. (2000). *Langmuir* **16**, 3703–3711.
- Renggli, D., Alicke, A., Ewoldt, R. H. & Vermant, J. (2020). *J. Rheol.* **64**, 141–160.
- Reynaert, S., Brooks, C. F., Moldenaers, P., Vermant, J. & Fuller, G. G. (2008). *J. Rheol.* **52**, 261–285.
- Rivière, S., Hénon, S., Meunier, J., Schwartz, D. K., Tsao, M.-W. & Knobler, C. M. (1994). *J. Chem. Phys.* **101**, 10045–10051.
- Sanchez-Puga, P. & Rubio, M. A. (2025a). *Comput. Phys. Commun.* **310**, 109499.
- Sanchez-Puga, P. & Rubio, M. A. (2025b). *psanchez0046/dwr-drag: Dwr-drag*, <https://doi.org/10.5281/zenodo.16459609>.
- Sanchez-Puga, P., Tajuelo, J., Pastor, J. M. & Rubio, M. A. (2019). *Comput. Phys. Commun.* **239**, 184–196.
- Sanchez-Puga, P., Tajuelo, J., Pastor, J. M. & Rubio, M. A. (2021). *Adv. Colloid Interface Sci.* **288**, 102332.
- Singh, P. K., Soulages, J. M. & Ewoldt, R. H. (2019). *Rheol. Acta* **58**, 341–359.
- Stoica, P. & Moses, R. L. (2005). *Spectral Analysis of Signals*, Vol. 452. Upper Saddle River: Pearson Prentice Hall.
- Tajuelo, J., Pastor, J. M., Martínez-Pedrero, F., Vázquez, M., Ortega, F., Rubio, R. G. & Rubio, M. A. (2015). *Langmuir* **31**, 1410–1420.
- Tajuelo, J., Pastor, J. M. & Rubio, M. A. (2016). *J. Rheol.* **60**, 1095–1113.

- Tajuelo, J., Rubio, M. A. & Pastor, J. M. (2018). *J. Rheol.* **62**, 295–311.
- Tein, Y. S., Thompson, B. R., Majkrzak, C., Maranville, B., Renggli, D., Vermant, J. & Wagner, N. J. (2022). *Rev. Sci. Instrum.* **93**, 093903.
- Thompson, B. R., Pham, K. G., Phan, M. D., Sanchez-Puga, P., Gutfreund, P., Wang, T., Qian, K. K., Heinrich, F., Liu, Y. & Wagner, N. J. (2025). *Appl. Mater. Interfaces* **17**, 40116–40128.
- Vandebril, S., Franck, A., Fuller, G. G., Moldenaers, P. & Vermant, J. (2010). *Rheol. Acta* **49**, 131–144.
- Verwijlen, T., Moldenaers, P., Stone, H. A. & Vermant, J. (2011). *Langmuir* **27**, 9345–9358.
- Vutukuri, H. R., Hoore, M., Abaurrea-Velasco, C., van Buren, L., Dutto, A., Auth, T., Fedosov, D. A., Gompper, G. & Vermant, J. (2020). *Nature* **586**, 52–56.
- Waldie, S., Sebastiani, F., Browning, K., Maric, S., Lind, T. K., Yepuri, N., Darwish, T. A., Moulin, M., Strohmeier, G., Pichler, H., Skoda, M. W., Maestro, A., Haertlein, M., Forsyth, V. T., Bengtsson, E., Malmsten, M. & Cárdenas, M. (2020). *Biochim. Biophys. Acta* **1865**, 158769.
- Zell, Z. A., Mansard, V., Wright, J., Kim, K., Choi, S. Q. & Squires, T. M. (2016). *J. Rheol.* **60**, 141–159.